Photodetectors Based on Lead Sulfide Quantum Dot and Organic Absorbers for Multispectral Sensing in the Visible to Short-Wave Infrared Range

Vladimir Pejović, Epimitheas Georgitzikis, Itai Lieberman, Paweł E. Malinowski, Paul Heremans, David Cheyns*

V. Pejović, E. Georgitzikis, I. Lieberman, P. E. Malinowski, P. Heremans, D. Cheyns
IMEC VZW Kapeldreef 75, 3001 Heverlee, Belgium
E-mail: vladimir.pejovic@imec.be

V. Pejović, P. Heremans
KU Leuven Kasteelpark Arenberg 10, 3001 Heverlee, Belgium

Keywords: PbS colloidal quantum dots, short-wave infrared, multispectral photodetectors, organic photodiodes

Multispectral imaging in short-wave infrared (SWIR) (1-2.5 μm range) is a powerful analytical technique because of distinctive spectral properties of many materials in this range. However, conventional SWIR image sensors are beyond the reach for many applications due to their high price. Thin-film image sensors based on colloidal quantum dots (CQDs) have been recently commercialized and are expected to deliver affordable infrared image sensors to a wider application scope. So far, the demonstrated CQD image sensors do not have a multispectral capability. Here, we present stacked, dual-band photodetector based on PbS CQDs. By engineering the surface of CQDs we fabricate two oppositely facing pn junctions in series, which enable sensing in two spectral channels. Furthermore, we design an optical cavity that reduces the spectral crosstalk between the two channels and simultaneously enables wavelength-tunability in one channel. Finally, we integrate an organic photodiode (OPD) with a PbS CQD photodiode in a single device, leveraging a high sensitivity in visible and near infrared (NIR) characteristic for OPDs. The presented photodetectors exhibit low dark current below 500 nA/cm^2 at 1 V bias, fast response measured in microseconds, as well as high external quantum efficiency reaching 70% in NIR and 30% in SWIR.

1. Introduction

Short-wave infrared (SWIR) is a range of electromagnetic radiation with wavelengths between 1 μm and 2.5 μm and it cannot be detected by traditional complementary metal-oxide-semiconductor (CMOS) photodiodes due to the absorption cut-off of silicon in near infrared (NIR). Traditionally, SWIR imaging is dominated by image sensors based on II-VI and III-V semiconductors such as InGaAs or HgCdTe, typically in focal plane array (FPA) configuration. [1–4] Despite their maturity, low-throughput fabrication on small wafers and complex integration with readout electronics prevents their wider application and keeps them reserved for niche domains.

Thin-film photodetectors based on colloidal quantum dots (CQDs) have been demonstrated as a promising technology to enable long-awaited affordable imaging in SWIR, which is necessary to support the development of emerging technologies such as AR/VR, autonomous driving, machine vision and others. [5] CQDs are chemically synthesized nanocrystals of which the bandgap can be tuned by adjusting their size, thanks to the quantum confinement effect. A wide range of CQDs that can absorb wavelengths longer than 1 μm have been synthesized, including PbS, PbSe, InAs and HgTe. [6–9] Various optoelectronic devices employing CQDs have been demonstrated, including solar cells, photodetectors and LEDs. [10–12] Monolithic integration of CQD photodetectors on readout integrated circuits (ROICs) enabled SWIR image sensors with unprecedented resolution and pixel density, with pixel pitch below 2 μm, outperforming conventional FPAs in this aspect. Several companies have already commercialized CQD-based imaging technology, offering products with high external quantum efficiency (EQE), high resolution and lower cost compared to traditional infrared FPAs. [5]

Semiconductor absorbers used in image sensors are characterized by a broadband absorption with a cut-off determined by the energy bandgap of the semiconductor material. For consumer applications, trichromatic red-green-blue (RGB) output that matches human vision is achieved by adding color filters on top of CMOS image sensors. Many industrial applications require imaging beyond standard RGB imaging. One common approach to divide the spectrum into more narrower bands is by utilizing optical filters based on Fabry-Perot cavities. [13,14] Depending on the number of available bands, this technique is called multispectral or hyperspectral imaging and it enables simultaneous collection of spatial and spectral information. When done in SWIR, multispectral imaging presents a powerful technique for chemical identification, thanks to a strong absorption fingerprint of many chemical compounds such as fats, proteins, water, etc. This is attractive for many applications in food industry, medicine, plastic sorting and many more. [15–19] However, integration of optical filters on top of FPAs further complicates the slow and costly integration and degrades the already low spatial resolution. Hence, enabling multispectral imaging in SWIR with CQDs is an attractive route for making this technology widely available.

CQD-based image sensors could, in principle, be upgraded for multispectral/hyperspectral imaging by integrating conventional transmission optical filters on top of thin-film pixels. However, multiple photolithography steps would have to be performed on top of delicate thin-film photodetectors in order to fabricate filters, which would be a rather challenging task. Moreover, spectral imaging requires a sensor with a high EQE in a broad range, such that sufficient sensitivity at different wavelengths of interest is maintained even when transmission filters are integrated on top of them, which inevitably reduce the overall sensitivity due to optical losses. CQD absorbers are relatively thin (typically up to 500 nm), and optical interference is exploited to enhance EQE. Although this method can lead to high EQE of even 80%, [20,21] it is measured at wavelengths where constructive interference occurs, and typically around CQD’s excitonic peak where the absorption coefficient is high. This directly leads to a situation in which EQE is low at the wavelengths where destructive interference occurs. Adding transmission filters on a CQD sensor with a typical EQE curve would yield unacceptably low sensitivity for a significant part of the operating spectral range. Hence, we chose to exploit the versatility of thin-film devices and develop a photodetector that enables detection of two separate bands, while maintaining the same integration complexity of standard CQD-based image sensors.

Although the majority of conventional multispectral imaging solutions operate in multiple bands (e.g., 4, 9, 16 or more), we posited that an upgrade from the current monochromatic broadband CQD imagers to a dual-band mode of operation would be beneficial and attractive for many applications. For example, the atmospheric absorption of photons with wavelengths around 1400 nm makes excellent conditions for active imaging, whereas abundant photons around the 1550 nm wavelength coming from the sun are ideal for passive imaging. [22] Having access to these two bands simultaneously, but separately, would make a robust imaging system. Moreover, several other wavelengths which are already well established in the industry are of high interest and can be paired with each other in a single image sensor, such as 940 nm or 1300 nm. Another example is cancer surgery in which access to visible photons is required for imaging the body, whereas infrared photons from fluorescent dyes help cancer identification.

Since the signals coming from the two sources are highly different in intensity, the readout electronics could be configured such that both signals can be detected optimally. [23]

2. Dual-Band Sensing with PbS CQDs

For this work, we chose PbS CQDs as the most mature and widely investigated type of CQDs for photodetection and imaging, which exhibits the highest performance in SWIR at the moment of writing and has already found its place in commercial products. [5] We realized the dual-band operation by developing a switchable photodetector for visible-SWIR range by vertically stacking two PbS CQD-based photodiodes. An advantage of the vertically stacked structure from the imaging point of view is a higher spatial resolution compared to conventional multispectral image sensors in which pixels are configured next to each other.

The concept of the switchable dual photodetector has been demonstrated in various technologies, both conventional bulk semiconductors, as well as thin-film materials. In the case of bulk semiconductors such as InP and InGaAs, [24,25] an important design consideration is crystal lattice matching, which limits the number of possible material combinations. On the other hand, the nature of thin-film processing enables a less stringent approach, without the necessity for lattice matching. A wide range of materials such as CQDs, organic semiconductors, metal-oxides and metals can be deposited in the same thin-film device stack. However, it should be noted that the processing of such devices must be orthogonal, meaning that the materials and used deposition techniques must be compatible with each other so that the underlying layers are not damaged or washed away during the deposition of new ones.

The first dual-photodiode structure intended for multispectral photodetection based on thin films was published by Tang et al. In this work, they fabricated a dual-band photodetector by using HgTe CQDs of two different sizes, which allowed capturing of SWIR and mid-wave infrared (MWIR) spectra separately, under low-temperature conditions. [26] Similar switchable photodetector devices based on organic and perovskite materials were reported. [27–29] A clear advantage of CQDs is the possibility to tune their bandgap for absorption in SWIR and beyond, which is still difficult for the other solution-processed semiconductors. Here, we focus on uncooled operation in the visible to SWIR range and use PbS CQDs.

2.1. Electrical Design

The presented photodetector is based on a two-terminal device that consists of two photodiodes in a back-to-back, serial connection (**Figure 1**). The two CQD photodiodes (CQDPDs) are made of nanocrystal absorbers of different sizes i.e., different bandgaps. By controlling the polarity of the bias voltage, either side of the photodetector can be activated, and a different part of the spectrum can be detected due to the difference in the absorption spectra of the two photodiodes. The electric field of the reverse-biased photodiode separates photo-generated electron-hole pairs, supplying a current through the device, whereas the other photodiode in the forward bias enables current flow.

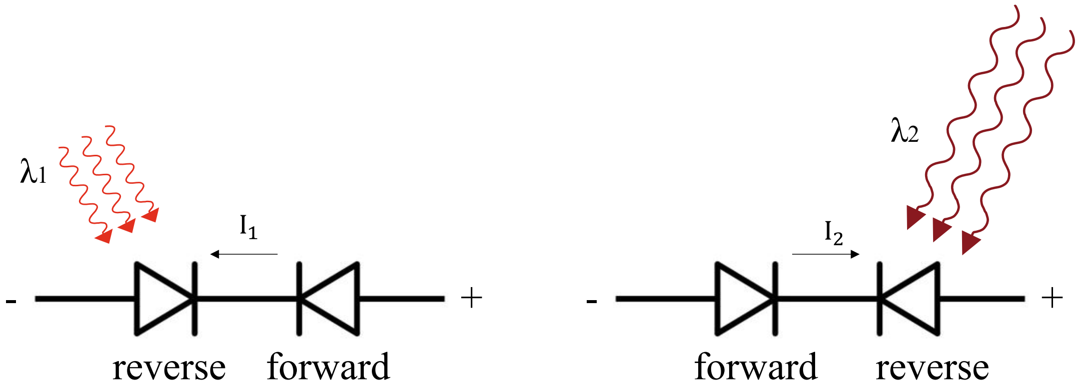

Figure 1. Concept illustration: one photodiode acts as a photodetector at a time and the change in the bias polarity switches the roles, enabling detection of two different spectral bands.

Depending on the order of fabrication of constituent layers, we propose two types of thin-film devices for dual-band photodetection: pn-NP (**Figure 2**a) and np-PN (Figure 2b). Both consist of two oppositely facing pn junctions in contact with each other, where capitalized letters denote the larger bandgap. The absorber with the wider bandgap should be positioned at the front, such that it is exposed to the light first and it should act as a pass filter for longer wavelengths.

In this work, we created pn junctions that consist of CQDs of different doping type, which causes a built-in field at the CQD-CQD interface. [30,31] It is well known that surface chemistry plays a key role in determining physical properties of CQD films, including doping density. [32,33] Insulating long chain alkyl ligands surrounding the surface of PbS CQDs introduced during the synthesis need to be replaced with shorter ligands to increase films' conductivity, in the process called ligand exchange. Depending on the choice of the new shorter ligands and the atmospheric conditions under which the ligand exchange process is performed, the doping type can be controlled, as well as the doping density (to a certain degree). Organic ligands containing thiol groups such as ethandithiol (EDT) and benzenedithiol (BDT), as well as exposure of CQDs to oxygen lead to p-type behavior. On the other hand, ionic ligands such as tetrabutylammonium iodide (TBAI), lead halides (PbI_2 and $PbBr_2$) or zinc iodide (ZnI_2), and inert atmosphere typically lead to n-type behavior.

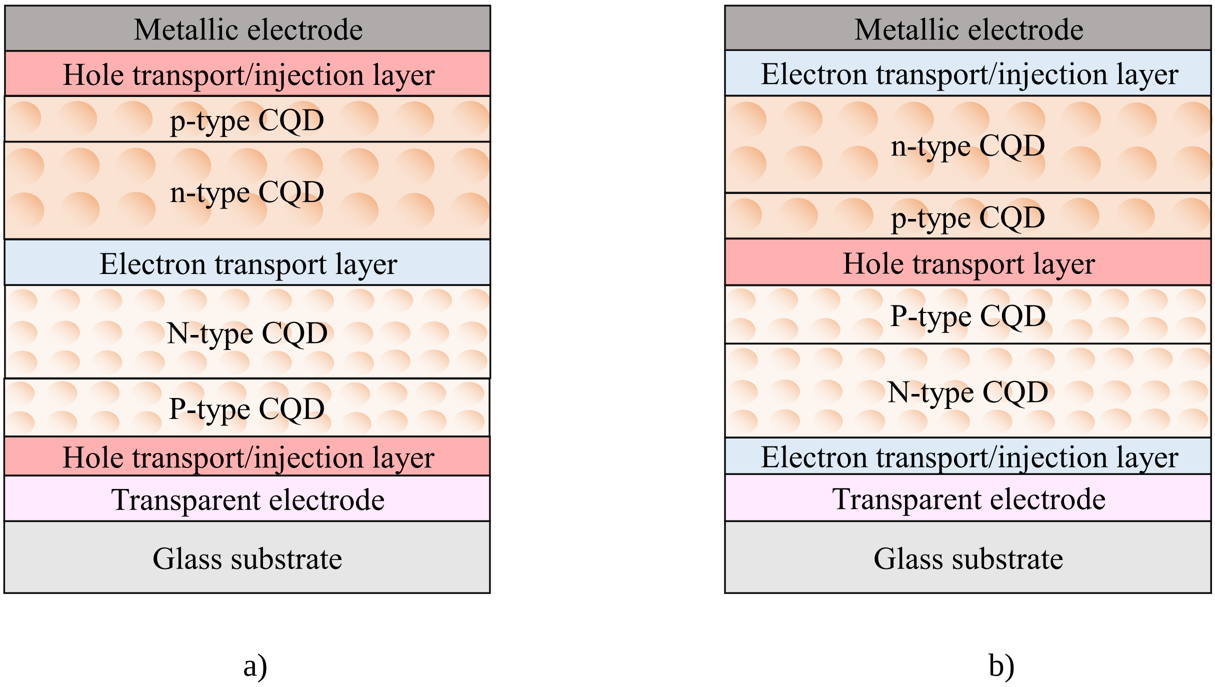

Figure 2. Illustration of two different PbS CQD photodetector structures for realization of dual-band photodetection: (a) pn-NP and (b) np-PN

In addition to the absorbers that form pn junctions, transport/injection layers can be added in the stack to aid charge carrier transport or reduce the dark current. For hole transport layer (HTL)/hole injection layer (HIL) materials such as poly(3,4-ethylenedioxythiophene) polystyrene sulfonate (PEDOT: PSS) or molybdenum oxide (MoOx) can be used. Alternatively, wide bandgap organic HTL such as Poly(N,N'-bis-4-butylphenyl-N,N'-bisphenyl)benzidine (PolyTPD) can be used to reduce the dark current because of its good electron blocking properties. [34] Metal oxides such as ZnO and TiO_2, either in form of nanoparticles or amorphous (e.g. sputtered) are a good choice for electron transport layers (ETLs)/electron injection layers (EILs), due to the favorable energy alignment with CQDs and their mechanical and chemical robustness, as well as good hole blocking properties. [35] Transport layers must be chosen carefully such that their energy band levels allow for extraction of photogenerated carriers, but also do not hinder injection of carriers from electrodes in forward bias which is necessary to support the photocurrent coming from the reverse biased photodiode. Semi-transparent electrode such as ITO is used on the illumination side of the stack, and a metallic reflective electrode on the opposite side. The electrode materials must be considered such that injection of charge carriers into transport layers under forward bias is efficient.

The principle of operation is illustrated in the band diagrams in **Figure 3** for the np-PN example. Under illumination and positive bias, electron-hole pairs generated in the photodiode with larger bandgap are separated by the electric field. Electrons are transferred via ETL to the electrode, whereas holes are transferred via HTL to the other photodiode which is in forward bias. These holes then recombine with the electrons that are injected from the electrode via the ETL on the opposite side, maintaining the current flow. The roles of the photodiodes switch when the polarity of the bias is changed. Analogously, the operation of the pn-NP structure can be explained following the same reasoning.

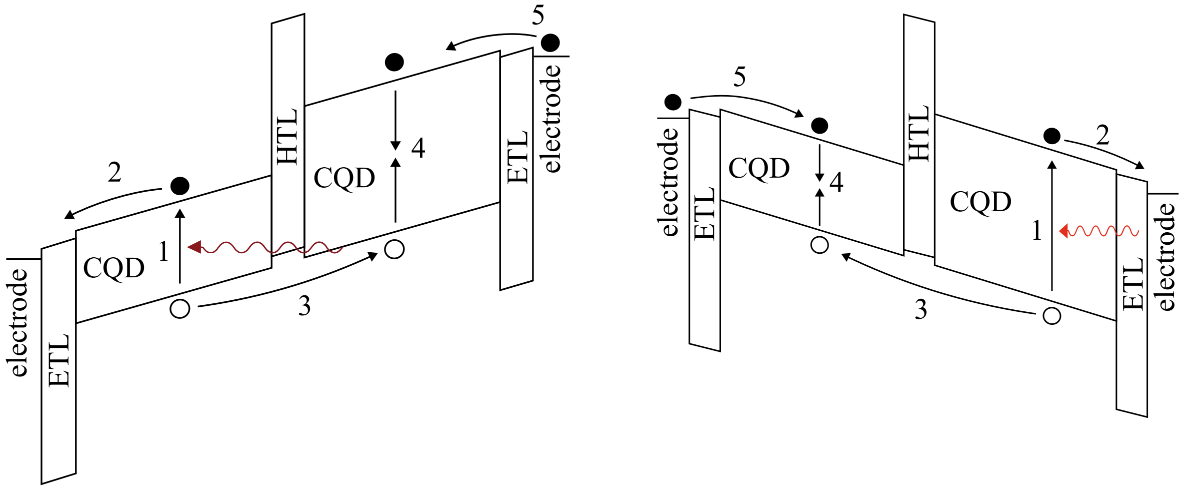

a)

b)

Figure 3. Illustrated band diagrams of dual-band photodetectors: (a) incident photons are absorbed and generate electron-hole pairs (process 1) in the narrow-bandgap photodiode, driven by the electric field, electrons are swept via ETL to the electrode (process 2), whereas holes are swept via HTL (process 3) to the forward biased wider-bandgap photodiode where they recombine with holes (process 4) that are injected (process 5) from the other electrode. (b) When bias polarity is switched, the photodiodes switch the roles: electron-hole pairs are generated in the wider-bandgap photodiode (process 1), electrons are swept to the electrode via ETL (process 2) and holes to the other photodiode via HTL (process 3) where they recombine (process 4) with the electrons injected (process 5) from the opposite electrode.

2.2. Optical Design

In order to fully understand and optimize the devices we performed optical simulations of the full dual-band photodetector stack. We characterized PbS CQDs films and transport layers by ellipsometry and extracted wavelength-dependent refractive index and extinction coefficient, which we plugged into an optical simulator based on a transfer matrix method.

For a successful operation of the switchable dual-band photodetector, it is required that the front photodiode with the wider-bandgap absorber efficiently filters the incoming light so that only light with longer wavelengths that cannot be absorbed in the front photodiode reaches the back photodiode. Due to the low mobility in PbS CQD films, diffusion length, hence absorption thickness is typically limited to a few hundred nanometers. In standard thin-film photodetectors and solar cells, the limited absorption path is partially compensated by exploiting back reflection from the metal electrode and optical interference. [36,37] However, in the dual-band photodetector discussed here, the metallic electrode is placed behind the lower-bandgap back photodiode. Hence, the light not absorbed in the first pass in the wider-bandgap front photodiode 'leaks' to the back photodiode, resulting in an inevitable spectral crosstalk (**Figure 4**a), which is undesirable and undermines the purpose of dual-band sensing.

To estimate the required thickness for efficient filtering, we simulated single-pass absorption of a PbS CQD film with the excitonic peak at 940 nm, as a function of the films thickness. For an absorber with thickness around 1 μm, the absorption at 940 nm is between 60% and 70% (Figure 4b). For more realistic thicknesses (e.g. 500 nm), the absorption drops to roughly 50%. At wavelengths outside of the excitonic peak where the absorption coefficient of PbS CQD is lower, the issue is more severe. Even with 1 μm thick absorber, which to our knowledge is the thickest reported in the literature, [38] the results would not be satisfactory. Hence, we sought alternative solutions.

To solve the problem of the spectral crosstalk, we propose a method with which we can optically decouple the two photodiodes, while maintaining the electrical operation. By inserting a semi-transparent mirror, such as thin silver (10-30 nm) between the two photodiodes, the back photodiode is placed inside a Fabry-Perot optical cavity formed between the silver layer and the back metal electrode (Figure 4c). Resonant wavelengths of the cavity are given by the equation:

$$k\lambda = 2nL\cos\theta$$

where k is the order of resonance, λ is the resonant wavelength, n is the effective refractive index of the cavity, L is the cavity thickness, and θ is the incident angle.

We simulated reflection from such cavity comprised of the photodiode stack with a 20 nm thick Ag and we varied the thickness of the absorber in the cavity (Figure 4d). In the narrow regions around the resonant wavelengths, light can penetrate the cavity where it can be absorbed by

CQDs. Outside of the resonant wavelengths, the light is effectively reflected from the cavity. Hence, the effect of the introduced silver layer is twofold: (1) it enhances light absorption in the front photodiode by reflecting the light not absorbed in the first pass, reducing the spectral crosstalk, and (2) it allows for tuning of the absorption (i.e. EQE) peak position of the back photodiode. It should be noted that the inserted silver film can be left floating i.e., no external electrical access is needed for the operation. Hence, the proposed modification of the structure does not complicate the fabrication procedure substantially. However, an efficient charge carrier transport in both directions must be maintained for a proper operation.

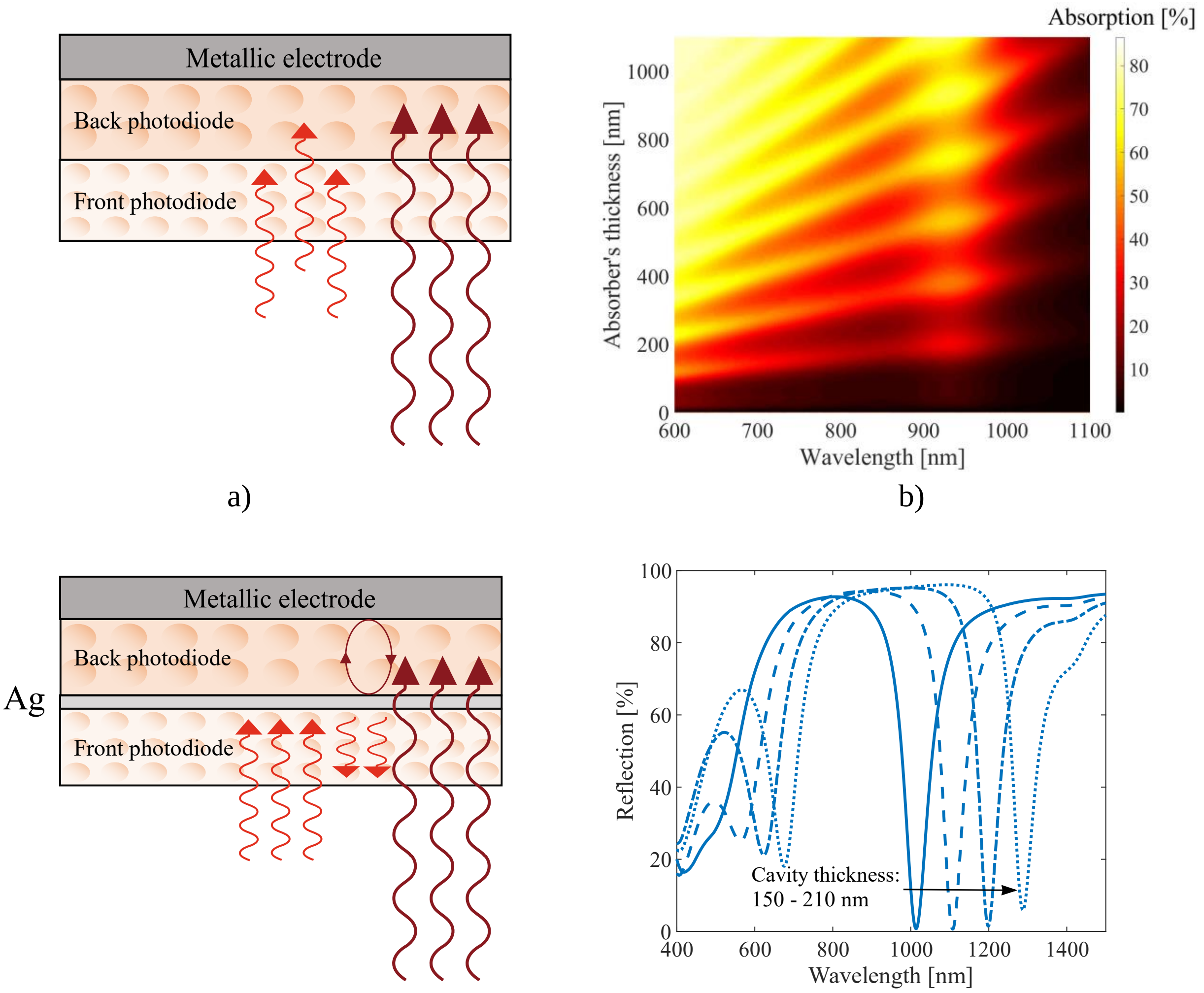

a)

b)

c)

d)

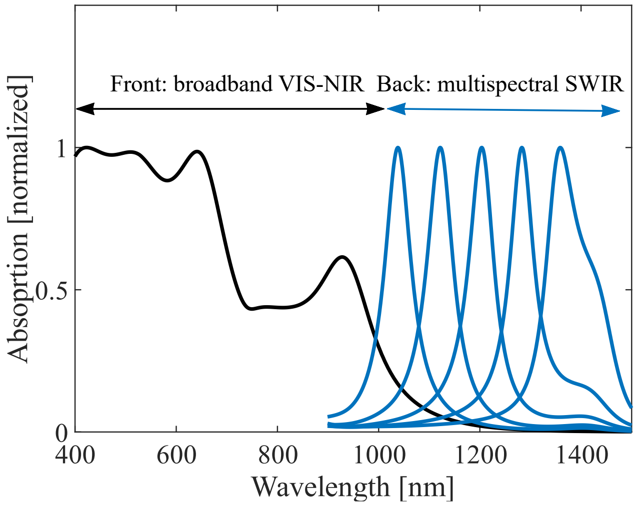

e)

Figure 4. (a) Illustration of the spectral crosstalk in a CQD dual-band photodetector. (b) Absorption of a single PbS CQD film as a function of the film's thickness and wavelength. (c) Modified dual-band photodetector structure for reduction of the spectral crosstalk. (d) Simulated reflection from an optical cavity with a CQD absorber inside the cavity. (e) Simulated absorption of a dual-band photodetector with a modified structure.

The effectiveness of the cavity is reduced for the visible range due to the decrease of silver's reflectivity. However, the spectral crosstalk in this range is not very pronounced because the absorption coefficient of CQDs is 3-8 times higher in the visible range compared to the NIR range, hence a single pass efficiently filters majority of the visible light.

With this method, we create a dual-band photodetector which can be used for broadband detection in one channel e.g., for the visible-NIR range, and another tunable channel for the SWIR range that can be tailored to a specific application. The spectral region between the two excitonic peaks in the absorption spectra of the used absorbers is a window within which the back photodiode can be tuned (Figure 4e). One can imagine an image sensor based on this kind of photodetector where a visible image (or visible-NIR) is overlaid with a multispectral image coming from several narrow bands in SWIR which can be tuned to specific applications.

3. Results and Discussion

All samples reported in this work were prepared on transparent glass substrates with pre-patterned ITO electrodes through which the devices are illuminated. We used two different sizes of PbS CQDs with excitonic absorption peaks at 940 nm and 1450 nm (**Figure S1**), which are the wavelengths with numerous applications in the industry. In the rest of the paper, we refer to two individual photodiodes that form the whole dual-band photodetector as front photodiode (940 nm excitonic peak) and back photodiode (1450 nm excitonic peak). Each photodiode contained a thinner (40 nm for the front and 90 nm for the back photodiode) p-type film obtained by using thiol ligands and air exposure, and a thicker (200 nm for the front and variable 200-350 nm for the back photodiode) n-type film obtained using iodide ions. The n-type film is thicker compared to the p-type film because of better charge carrier transport properties of n-type PbS CQD films in general. [39–41] Spin-coating and solid-state ligand exchange process were performed for all CQD layers, which involves soaking PbS film in a ligand solution. This approach allowed stacking multiple distinct CQD layers on top of each other, without damaging the underlying layers. The fabrication process is further detailed in the Experimental Section.

Firstly, we attempted to implement the cavity effect in a pn-NP structure by placing a silver film between two ETLs in the middle of the photodetector (**Figure S2**). The reference device without the silver film exhibited photodetection functionality at both voltage polarities, albeit with high spectral crosstalk, as predicted by the simulations (**Figure S3**). However, the devices with the inserted thin silver film did not show any measurable EQE, indicating that the silver film disrupts the electrical operation. We posited that electron injection from silver to the ETL in the middle of the photodetector is not efficient, which disrupts the current balance between the two constituent photodiodes, resulting in an unfunctional device. Replacing the silver layer with an aluminum layer which has low work function suitable for electron injection is not a viable option because of the too high optical losses in aluminum. Hence, we decided to switch to the np-PN structure in which the middle silver layer serves as a hole recombination and hole injection layer.

In order to enable efficient hole transport from one photodiode to the other, we placed the silver layer between two MoOx layers which is known as a good hole extraction and hole injection material (**Figure 5**a). [42,43] Moreover, MoOx has been demonstrated as a good seed material for growth of silver. [44] Photo-generated holes move towards the silver film via MoOx, where they recombine, while the other MoOx layer serves as a hole injection layer, keeping the currents in the photodetector balanced (Figure 5b). In addition, we deposited a PolyTPD HTL between the MoOx layer and the P-type CQDs in the front photodiode in order to reduce the dark current caused by injection of carriers from the inserted silver film under reverse bias.

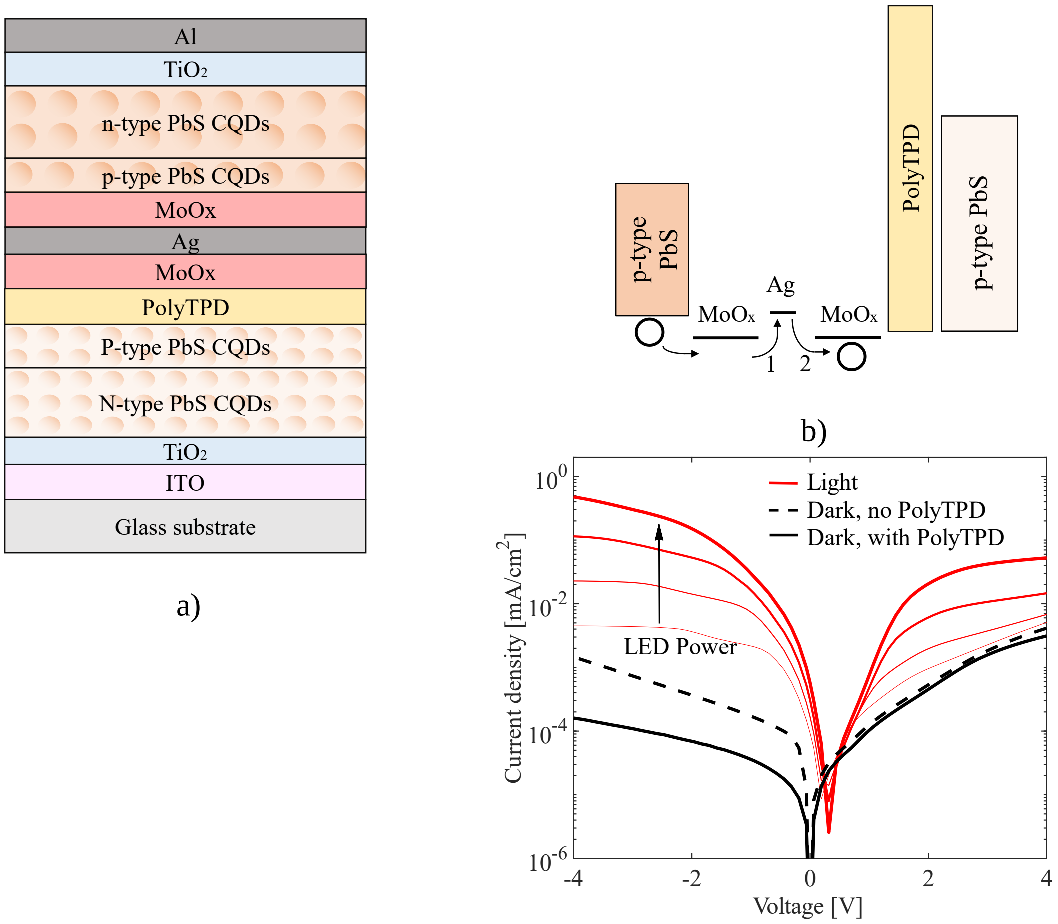

a)

b)

c)

Figure 5. (a) Thin-film stack of the np-PN dual-band photodetector with a middle thin silver film. (b) The illustrated band diagram shows recombination (process 1) and injection (process 2) of holes in the silver layer that maintain the current flow. (c) Current density-voltage characteristics of the dual-band photodetector under dark and light conditions.

The obtained JV curves under dark and light conditions are shown in Figure 5c, demonstrating that the middle silver layer does not disrupt the operation in the pn-NP structure. At both positive (back photodiode actived) and negative (front photodiode actived) voltage bias, an effective photodetection functionality is observed with a high difference between the currents under dark (black curves) and light (red curves) conditions.

We observed that the insertion of the silver film increases the dark current of the front photodiode by an order of magnitude, whereas the increase in the case of the back photodiode is negligible (**Figure S4**). We posit that the dark current of the back photodiode is dominated by the generation in the absorber and the injection from the silver film under reverse bias is screened by the generation current. However, due to the wider bandgap, generation current of the front photodiode is lower and the injection from the silver has a more significant impact. Hence, we included the PolyTPD layer in the front photodiode and effectively limited the injection from the silver film (dashed versus solid black curves in Figure 5c).

Our simulations suggested that the EQE of the back photodiode in a cavity can be tuned independently of the broadband front photodiode (**Figure S5**), which is a convenience that facilitates the design process. Hence, we fabricated a range of single photodiodes with the MoOx-Ag (25 nm)-MoOx electrode on the illumination side, equivalent to the back photodiode used in the dual-band configuration, in order to verify the resonance effect experimentally. **Figure 6**a shows EQE measured for devices with different cavity thicknesses obtained by varying the thickness of the CQD absorber, plotted together with the extinction coefficient of the used CQDs. Various EQE peaks can be observed at different wavelengths, without any corresponding peaks in the extinction coefficient curve. Hence, the conclusion is that the EQE peaks originate from the light resonance in the cavities. The obtained EQE values at resonant wavelengths are in the 7-17% range, with a downward trend with increasing wavelength. This trend can be explained by the reduction in the extinction coefficient of PbS CQDs, but also by the reduced efficiency of carrier extraction in thicker absorbers.

The 2nd order resonant peaks occurring at shorter wavelengths can potentially cause spectral crosstalk. However, we fabricated a full double photodiode stack with the back photodiode in a cavity and observed that the front photodiode dominantly absorbs in the 0.4-1.1 µm range, and that the spectral crosstalk is largely reduced (solid curves in Figure 6b) compared to the equivalent device without the thin silver (dashed curves in Figure 6b), which exhibits a high overlap in the two spectra. The EQE of the back photodiode is suppressed in the wide range except at the wavelengths determined by the cavity. As predicted, in addition to the lowered crosstalk, the EQE measured from the front photodiode is increased due to the reflection from the cavity, except in the 400 – 600 nm region which is caused by the optical losses in the added silver film. A certain degree of the spectral crosstalk due to the back photodiode’s absorption at the higher order resonant wavelength remains, but with the narrow peak and low EQE of less than 10% at 790 nm, the crosstalk is significantly lower compared to the reference case without the silver layer. With this, we demonstrate that we can independently optimize the back photodiode in the cavity and integrate it in a dual-photodiode device.

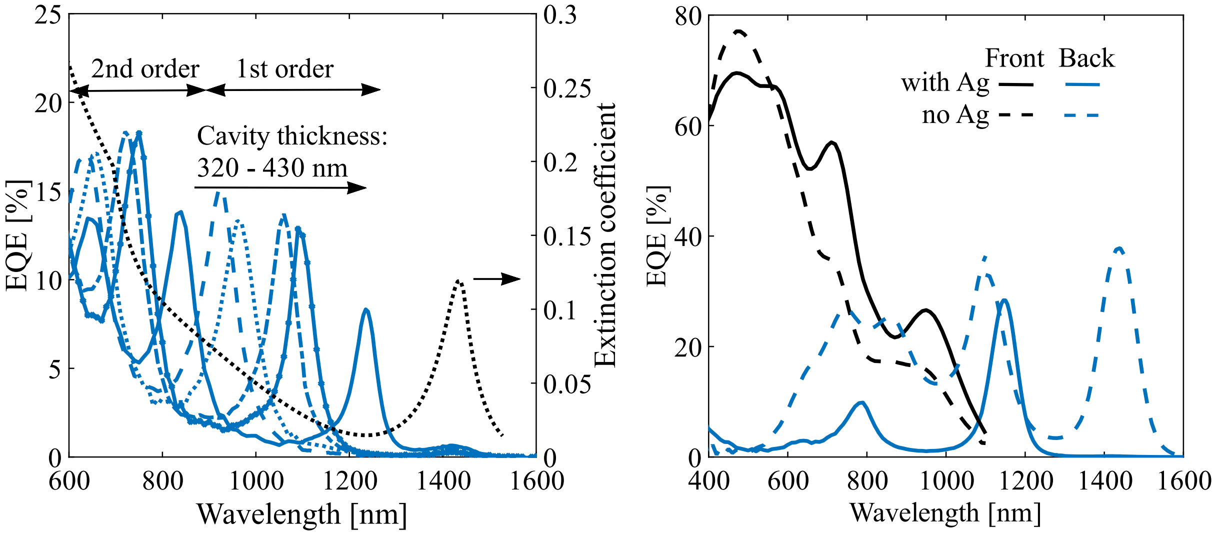

a) b)

Figure 6. (a) Measured EQE curves of single photodiodes in a cavity with a variable absorber's thickness (left axis) and the extinction coefficient curve of the used CQDs (right axis). (b) Measured EQE curves of the dual-band photodetector with (solid) and without (dashed) the middle thin silver film.

An important design parameter is the thickness of the middle thin silver film which affects the properties of the absorption peak – thicker films lead to narrower peaks (which is an important metric for multispectral applications) but also higher optical losses. Hence, a tradeoff has to be made between EQE and width of the peak. In the dual-band photodetector, we reduced the thickness of the silver layer from 25 nm used in single photodiodes to 20 nm and enhanced the EQE of the back photodiode to 28% at 1150 nm, sacrificing 20 nm in full width at half maximum (FWHM), compared to the single photodiodes in cavity we fabricated. FWHM could be improved by using thinner absorbers for example, as demonstrated by Wang et al. [45]

3.1. Combining Organics with Quantum Dots

Lastly, we implemented our approach to create hybrid photodetectors with CQD-organic absorbers. Organic photodiodes (OPDs) are attractive for imaging, for example in combination with flexible readouts, as well as for cointegration with organic light emitting diode (OLED) displays. [46,47] Moreover, they have shown impressive performance for the VIS-NIR range, delivering high EQEs and low dark currents measured in tens of pA/cm^2. [48] However, organic absorbers cannot deliver competitive EQE in SWIR. Hence, extending OPD's spectral range by integrating it with a tunable SWIR CQDPD could be an attractive option for many applications.

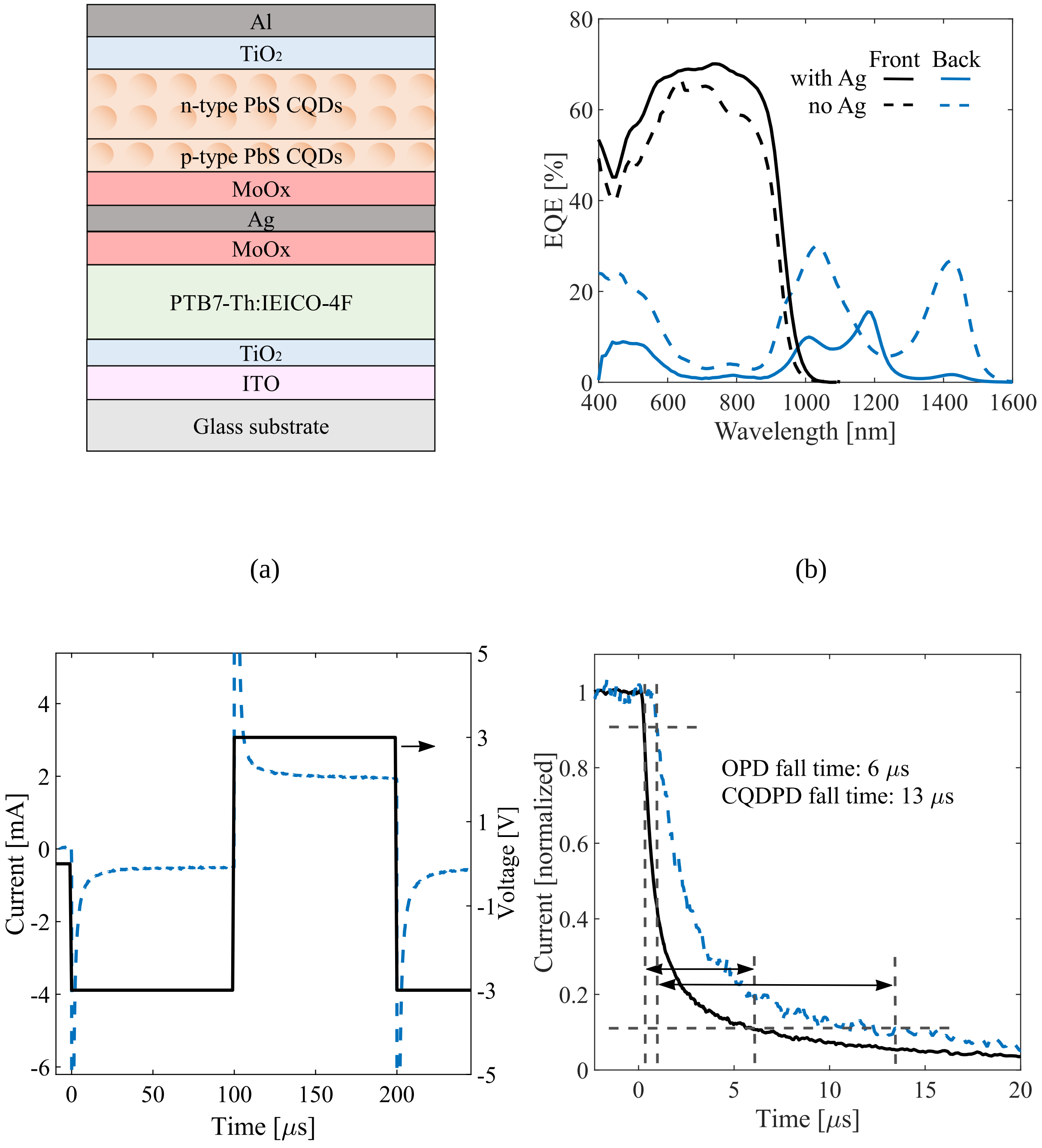

(a) (b)

(c) (d)

Figure 7. OPD-CQDPD dual-band photodetectors: (a) illustration of the device thin-film stack, (b) EQE curves with and without the middle Ag film. Transient behavior of OPD-CQDPD dual

band photodetectors: (c) transient photocurrent under constant illumination and pulsed voltage bias and (d) transient photocurrent under constant voltage bias and pulsed light signal.

In the previously shown np-PN structure, we replaced the front CQDPD by a bulk heterojunction photodiode based on PTB7-Th donor and IEICO-4F acceptor (**Figure 7**a), which has been already used for highly efficient photodetectors and image sensors. [49] We kept the same transport layers and deposited the organic absorber by spin-coating. The fabrication was done on glass substrates, starting with the OPD, which proved to be highly resistant to the subsequent evaporations and different solvents used for CQD fabrication.

Firstly, we measured JV (**Figure S6**) and EQE (Figure 7b) curves of the dual-band photodetector with the OPD, demonstrating an efficient photodetection in both photodiodes, with very high EQE across the VIS-NIR range coming from the OPD. We tested the middle MoOx-Ag-MoOx electrode, and it proved to be compatible with the OPD, reducing the spectral crosstalk and boosting the EQE in the NIR range to 70% (Figure 7b). The remaining spectral crosstalk in the visible could be further reduced by choosing another donor material with a higher absorption coefficient in the 400-600 nm range.

At the end, we performed two types of measurements to test the speed of operation, an important parameter for many applications. We measured transient photocurrent under constant illumination and pulsed bias voltage to obtain the switching speed between the two photodiodes (Figure 7c), as well as transient photocurrent under constant bias and pulsed light signal to obtain 90-10% fall time (Figure 7d). The photodetectors showed fast switching speed of 10 μs and fall time of 6 μs and 13 μs for the OPD and the CQDPD, respectively. The slower operation of the CQDPD’s and the observed delay of its photocurrent decay with respect to the OPD’s photocurrent can be attributed to the low charge carrier mobility and abundant trap states in PbS CQD films. [41,50,51]

4. Conclusion

In this paper, we presented dual-band photodetectors based on PbS CQDs and on OPD-PbS CQDs that enable multispectral sensing in a broadband region spanning from visible to SWIR. We showed how surface chemistry of PbS CQDs can be engineered to create two oppositely facing pn junctions that allow for bias-selective spectral response. With the optical simulations, we tackled the issue of spectral crosstalk and invented a crosstalk reduction method based on resonant optical cavities. We further exploited the cavity effect to upgrade our photodetector to a dual-band operation with one side being wavelength-tunable, expanding its potential applications. Finally, we combined the PbS CQDPD with an OPD optimized for the visible range, creating a possibility to capture visible light with very high efficiency together with SWIR light in a single vertically stacked device. This work exemplifies well how thin-film technologies can be used to achieve functionalities and architectures that are not easily achievable with conventional semiconductor technologies.

5. Experimental Section

Materials: All the chemicals were purchased from commercial suppliers. Smaller PbS CQDs were purchased from QustomDot and bigger dots from Quanutm Solutions. Solvents and ligands were purchased from Merck and polymers from 1-Material.

Device Fabrication: All devices were fabricated on glass substrates with pre-patterned ITO electrodes which were cleaned in ultrasonic bath using soap, water, acetone, and isopropanol. 20 nm thick TiO_2 ETL was deposited by electron-beam evaporation in Angstrom Engineering evaporator at 10^{-4} Torr and constant inflow of oxygen of 9 sccm. PbS CQD films were deposited by spin-coating solution of CQDs in octane (40 mg/ml and 50 mg/ml for bigger and smaller dots, respectively) at 2500 rpm for 15 s. Solid-state ligand exchange was performed on all CQD layers which consists of soaking a solid CQD film in a ligand solution, followed by spin-coating to dry the film. After that, the same pure solvent used for preparation of the ligand solution was dispensed over the whole substrate and immediately spun in order to wash the residual ligands. The washing process was repeated twice for each film. Recipes for ligand solutions were adopted from the literature. TBAI and EDT ligands were used for smaller dots, for n-type and p-type films, respectively. [52] ZnI_2-MPA mixture, and 1,4 benzenedithiol BDT were used for bigger dots, for n-type and p-type films, respectively. [21] The deposition and the solid-state ligand exchange process yield a thin film (25 nm for smaller dots and 30 nm for bigger dots) and in order to obtain sufficiently thick absorbers, the whole process was repeated multiple times. P-type layers were fabricated by deposition of two (smaller dots) and three (bigger dots) individual solid-state exchanged layers. N-type layers were fabricated by deposition of ten for smaller dots and variable number of layers (7-11) for bigger dots in order to tune the optical cavity. Deposition and ligand exchange were performed under inert conditions but after completion of each p-type part of the junction, the substrates were left overnight in a dry-air box to enhance p doping, and afterwards returned to the glovebox for the remaining fabrication steps. CQD layers were annealed for 10 min at 80˚ C under inert conditions. PolyTPD solution in chlorobenzene (6 mg/ml) layer was spincoated at 1000 rpm for 60 s and annealed at 80˚ C for 20 min. For the OPD, a mixture of PTB7-th and IEICO-4F (1:1.5 mass ratio) was dissolved in chlorobenzene (25 mg/ml) and spin-coated at 1000 rpm for 60 s under inert environment. 10 nm thick MoOx was deposited by thermal evaporation in Angstrom Engineering evaporator at 10^{-6} Torr. 100 nm thick top electrode (Al for np-PN and Ag for pn-NP structures) and middle Ag film were deposited by thermal evaporation at 10^{-6} Torr in Angstrom Engineering evaporator. The fabrication process for the single-band photodiodes was identical to the process followed for the fabrication of the back photodiode in the dual-band photodetector. PEDOT:PSS was used as an HTL of the front photodiode in the pn-NP structure (see Figure S2). It was spincoated at 5000 rpm for 60 s and annealed at 130˚ C under inert conditions for 10 min.

EQE Measurements: Spectral response measurements were performed using an in-house built setup. A light beam from a halogen source was coupled into a monochromator, giving a coverage over the spectral range of 400 –1800 nm. The light was chopped using a mechanical wheel and the signal from the photodetectors were collected by using a lock-in amplifier and a current preamplifier.

Current–Voltage Characterization and Transient Measurements: Current-voltage characteristic and transient behavior of the photodetectors were obtained using Fluxim's PAIOS system.

Ellipsometry: Optical constants and film thickness of the materials were measured using a Woollam ellipsometer.

Supporting Information

Supporting Information is available from the Wiley Online Library or from the author.

References

[1] A. Rouvié, J. Coussement, O. Huet, J. P. Truffer, M. Pozzi, E. H. Oubensaid, S. Hamard, V. Chaffraix, E. Costard, In *Infrared Technology and Applications XLI*, **2015**.

[2] M. MacDougal, J. Geske, C. Wang, D. Follman, In *Infrared Technology and Applications XXXVI*, **2010**.

[3] S. Manda, Y. Zaizen, T. Hirano, H. Iwamoto, R. Matsumoto, S. Saito, S. Maruyama, H. Minari, T. Hirano, T. Takachi, N. Fujii, Y. Yamamoto, In *Technical Digest - International Electron Devices Meeting, IEDM*, **2019**.

[4] R. Fraenkel, E. Berkowicz, L. Bikov, R. Elishkov, A. Giladi, I. Hirsh, E. Ilan, C. Jakobson, P. Kondrashov, E. Louzon, I. Nevo, I. Pivnik, A. Tuito, S. Vasserman, In *Infrared Technology and Applications XLIII*, **2017**.

[5] V. Pejovic, E. Georgitzikis, J. Lee, I. Lieberman, D. Cheyns, P. Heremans, P. E. Malinowski, *IEEE Transactions on Electron Devices* **2021**, 1.

[6] I. Moreels, K. Lambert, D. Smeets, D. de Muynck, T. Nollet, J. C. Martins, F. Vanhaecke, A. Vantomme, C. Delerue, G. Allan, Z. Hens, *ACS Nano* **2009**, *3*.
[7] I. Moreels, K. Lambert, D. de Muynck, F. Vanhaecke, D. Poelman, J. C. Martins, G. Allan, Z. Hens, *Chemistry of Materials* **2007**, *19*.
[8] M. Ginterseder, D. Franke, C. Perkinson, L. Wang, E. Hansen, M. Bawendi, **2020**.
[9] S. Keuleyan, E. Lhuillier, P. Guyot-Sionnest, *Journal of the American Chemical Society* **2011**, *133*.
[10] J. Tang, E. H. Sargent, *Advanced Materials* **2011**, *23*, 12.
[11] R. Saran, R. J. Curry, *Lead sulphide nanocrystal photodetector technologies*, Vol. 10, **2016**, pp. 81–92.
[12] S. Pradhan, F. di Stasio, Y. Bi, S. Gupta, S. Christodoulou, A. Stavrinadis, G. Konstantatos, *Nature Nanotechnology* **2019**, *14*, 72.
[13] A. Lambrechts, P. Gonzalez, B. Geelen, P. Soussan, K. Tack, M. Jayapala, In *Technical Digest - International Electron Devices Meeting, IEDM*, **2015**.
[14] N. Tack, A. Lambrechts, P. Soussan, L. Haspeslagh, In *Silicon Photonics VII*, **2012**.
[15] K. D. Hakkel, M. Petruzzella, F. Ou, A. van Klinken, F. Pagliano, T. Liu, R. P. J. van Veldhoven, A. Fiore, *Nature Communications* **2022**, *13*, 103.
[16] G. Lu, B. Fei, *Journal of Biomedical Optics* **2014**, *19*.
[17] R. H. Wilson, K. P. Nadeau, F. B. Jaworski, B. J. Tromberg, A. J. Durkin, *Journal of Biomedical Optics* **2015**, *20*.
[18] E. Alisaac, J. Behmann, A. Rathgeb, P. Karlovsky, H. W. Dehne, A. K. Mahlein, *Toxins* **2019**, *11*.
[19] F. Hollstein, M. Wohllebe, S. Arnaiz, In *Near Infrared Spectroscopy: Proceedings of the International Conference*, **2015**.
[20] M. Vafaie, J. Z. Fan, A. Morteza Najarian, O. Ouellette, L. K. Sagar, K. Bertens, B. Sun, F. P. García de Arquer, E. H. Sargent, *Matter* **2021**, *4*, 1042.
[21] Y. Bi, S. Pradhan, S. Gupta, M. Z. Akgul, A. Stavrinadis, G. Konstantatos, *Advanced Materials* **2018**, *30*.
[22] P. E. Malinowski, J. Lee, E. Georgitzikis, V. Pejovic, I. Lieberman, T. Ke, Y. Li, T. Verschooten, S. Thijs, A. D. Cheyns, *SID Symposium Digest of Technical Papers* **2021**, *52*.
[23] S. Blair, M. Garcia, T. Davis, Z. Zhu, Z. Liang, C. Konopka, K. Kauffman, R. Colanceski, I. Ferati, B. Kondov, S. Stojanoski, M. B. Todorovska, N. T. Dimitrovska, N. Jakupi, D. Miladinova, G. Petrusevska, G. Kondov, W. L. Dobrucki, S. Nie, V. Gruev, *Science Translational Medicine* **2021**, *13*.
[24] Z. Xie, Z. Deng, B. Chen, In *2020 Conference on Lasers and Electro-Optics Pacific Rim, CLEO-PR 2020 - Proceedings*, **2020**.
[25] Z. Xie, Z. Deng, X. Zou, B. Chen, *IEEE Photonics Technology Letters* **2020**, *32*.
[26] X. Tang, M. M. Ackerman, M. Chen, P. Guyot-Sionnest, *Nature Photonics* **2019**, *13*.
[27] B. Huang, J. Liu, Z. Han, Y. Gu, D. Yu, X. Xu, Y. Zou, *ACS Applied Materials and Interfaces* **2020**, *12*.
[28] J. Liu, Y. Zou, B. Huang, Y. Gu, Y. Yang, Z. Han, Y. Zhang, X. Xu, H. Zeng, *Nanoscale* **2020**, *12*.
[29] Z. Lan, F. Zhu, *ACS Nano* **2021**, *15*.
[30] J. Tang, H. Liu, D. Zhitomirsky, S. Hoogland, X. Wang, M. Furukawa, L. Levina, E. H. Sargent, *Nano Letters* **2012**, *12*.
[31] C. H. M. Chuang, P. R. Brown, V. Bulović, M. G. Bawendi, *Nature Materials* **2014**, *13*, 796.
[32] O. Voznyy, D. Zhitomirsky, P. Stadler, Z. Ning, S. Hoogland, E. H. Sargent, *ACS Nano* **2012**, *6*, 8448.
[33] A. Stavrinadis, G. Konstantatos, *Strategies for the Controlled Electronic Doping of Colloidal Quantum Dot Solids*, Vol. 17, **2016**.

[34] X. Zhou, D. Yang, D. Ma, *Advanced Optical Materials* **2015**, *3*.

[35] B. N. Pal, I. Robel, A. Mohite, R. Laocharoensuk, D. J. Werder, V. I. Klimov, *Advanced Functional Materials* **2012**, *22*, 1741.

[36] S. W. Baek, O. Ouellette, J. W. Jo, J. Choi, K. W. Seo, J. Kim, B. Sun, S. H. Lee, M. J. Choi, D. H. Nam, L. N. Quan, J. Kang, S. Hoogland, F. P. García De Arquer, J. Y. Lee, E. H. Sargent, *ACS Energy Letters* **2018**, *3*.

[37] E. Georgitzikis, P. E. Malinowski, J. Maes, A. Hadipour, Z. Hens, P. Heremans, D. Cheyns, *Advanced Functional Materials* **2018**, *28*.

[38] J. Z. Fan, M. Vafaie, K. Bertens, M. Sytnyk, J. M. Pina, L. K. Sagar, O. Ouellette, A. H. Proppe, A. S. Rasouli, Y. Gao, S. W. Baek, B. Chen, F. Laquai, S. Hoogland, F. P. G. de Arquer, W. Heiss, E. H. Sargent, *Nano Letters* **2020**, *20*.

[39] A. H. Proppe, J. Xu, R. P. Sabatini, J. Z. Fan, B. Sun, S. Hoogland, S. O. Kelley, O. Voznyy, E. H. Sargent, *Nano Letters* **2018**, *18*.

[40] X. Lan, O. Voznyy, A. Kiani, F. P. García De Arquer, A. S. Abbas, G. H. Kim, M. Liu, Z. Yang, G. Walters, J. Xu, M. Yuan, Z. Ning, F. Fan, P. Kanjanaboos, I. Kramer, D. Zhitomirsky, P. Lee, A. Perelgut, S. Hoogland, E. H. Sargent, *Advanced Materials* **2016**, *28*.

[41] E. Georgitzikis, J. Genoe, P. Heremans, D. Cheyns, *ACS Applied Materials and Interfaces* **2020**, *12*.

[42] X. Zhang, F. You, Q. Zheng, Z. Zhang, P. Cai, X. Xue, J. Xiong, J. Zhang, *Organic Electronics* **2016**, *39*.

[43] V. Shrotriya, G. Li, Y. Yao, C. W. Chu, Y. Yang, *Applied Physics Letters* **2006**, *88*.

[44] Z. Wang, C. Zhang, R. Gao, D. Chen, S. Tang, J. Zhang, D. Wang, X. Lu, Y. Hao, *Solar Energy Materials and Solar Cells* **2014**, *127*.

[45] J. Wang, S. Ullbrich, J. L. Hou, D. Spoltore, Q. Wang, Z. Ma, Z. Tang, K. Vandewal, *ACS Photonics* **2019**, *6*.

[46] A. Kumar, D. Moet, J.-L. van der Steen, A. Tripathi, F. G. Rodriguez, J. Maas, M. Simon, W. Reutten, A. Douglas, R. Raaijmakers, P. E. Malinowski, K. Myny, U. Shafique, R. Andriessen, P. Heremans, G. Gelinck, In *Organic Photonics VI*, **2014**.

[47] P. E. Malinowski, T. H. Ke, H. Akkerman, A. Nakamura, S. Shanmugam, A. van Breemen, D. vander Velpen, E. Vandenplas, L. M. Hagelsieb, L. Verscheuren, J. Genoe, W. Dehaene, A. J. Kronemeier, S. Steudel, G. Gelinck, P. Heremans, In *Digest of Technical Papers - SID International Symposium*, **2019**.

[48] C. Fuentes-Hernandez, W. F. Chou, T. M. Khan, L. Diniz, J. Lukens, F. A. Larrain, V. A. Rodriguez-Toro, B. Kippelen, *Science* **2020**, *370*.

[49] W. Yang, W. Qiu, E. Georgitzikis, E. Simoen, J. Serron, J. Lee, I. Lieberman, D. Cheyns, P. Malinowski, J. Genoe, H. Chen, P. Heremans, *ACS Applied Materials and Interfaces* **2021**, *13*.

[50] N. Yazdani, D. Bozyigit, O. Yarema, M. Yarema, V. Wood, *Journal of Physical Chemistry Letters* **2014**, *5*.

[51] S. Volk, N. Yazdani, O. Yarema, M. Yarema, V. Wood, *ACS Applied Electronic Materials* **2020**, *2*.

[52] C. H. M. Chuang, P. R. Brown, V. Bulović, M. G. Bawendi, *Nature Materials* **2014**, *13*.

Supporting information

Photodetectors Based on Lead Sulfide Quantum Dot and Organic Absorbers for Multispectral Sensing in the Visible to Short-Wave Infrared Range

Vladimir Pejović, Epimitheas Georgitzikis, Itai Lieberman, Paweł E. Malinowski, Paul Heremans, David Cheyns*

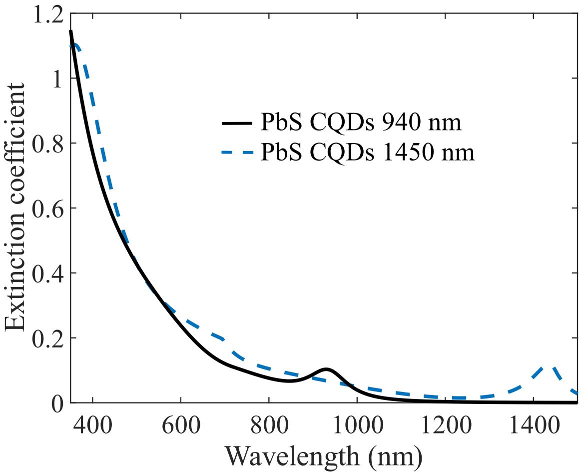

Figure S1. Extinction coefficient versus wavelength for the two different types of PbS CQDs used.

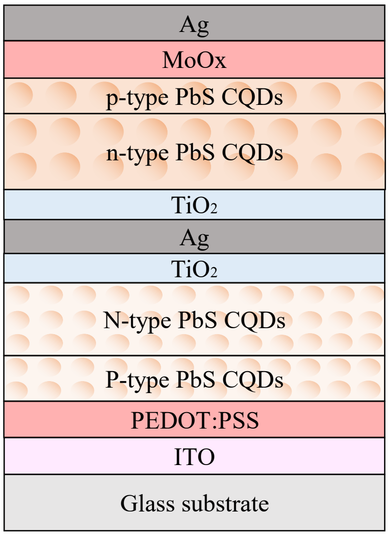

Figure S2. pn-NP stack illustration with a thin silver film in the middle.

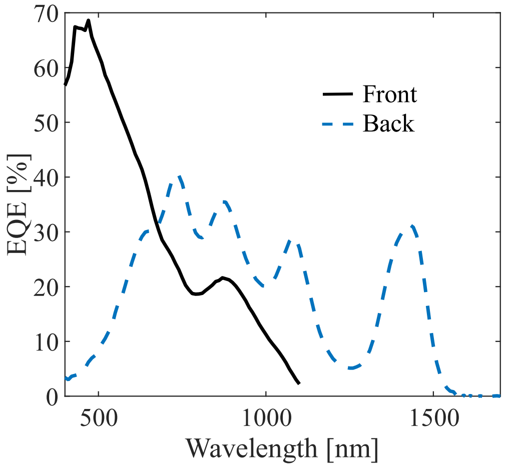

Figure S3. Measured EQE from a dual-band photodetector without a thin silver showing high spectral crosstalk between the two photodiodes.

When no thin silver is added in the middle to separate the two photodiodes, the whole dual-band photodetector is a single optical stack in which light interference occurs due to the back metallic electrode and it is impossible to limit the spectral crosstalk. In the EQE curves shown in Figure S3 measured from a pn-NP dual-band photodetector, it is clear that a high spectral crosstalk is present in the 600-1100 nm range.

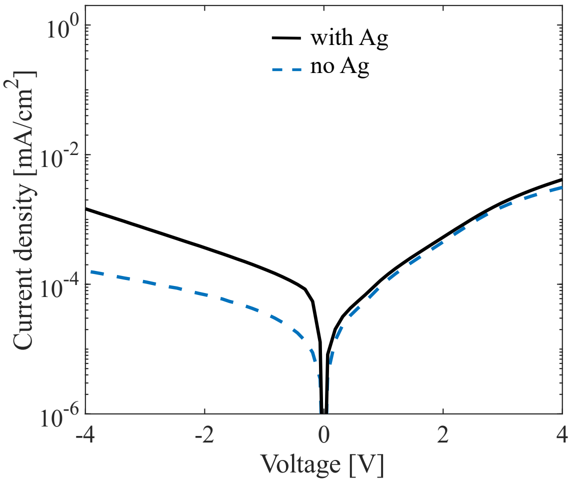

Figure S4. Current density versus voltage of the dual-band photodetector with and without the middle silver film inserted.

Simulations (Figure S5) show that the resonant peaks at wavelengths longer than 1 µm in the cavity do not change when the photodiode is integrated with a front photodiode because they are optically decoupled, which means that the two photodiodes can be optimized separately. At shorter wavelengths, the higher order resonant peaks are suppressed when a front diode is added. However, it should be noted that the simulations overestimate the absorption in the cavity because the roughness of the middle silver layer is disregarded. In reality, the absorption at all resonant wavelengths is lower.

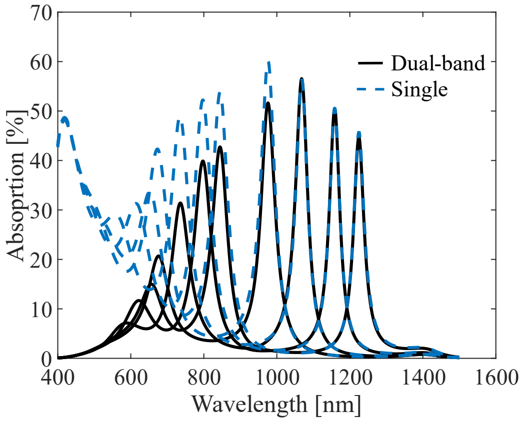

Figure S5. Simulated absorption of a back cavity photodiode in a dual-band photodetector and the equivalent device but as a single photodiode.

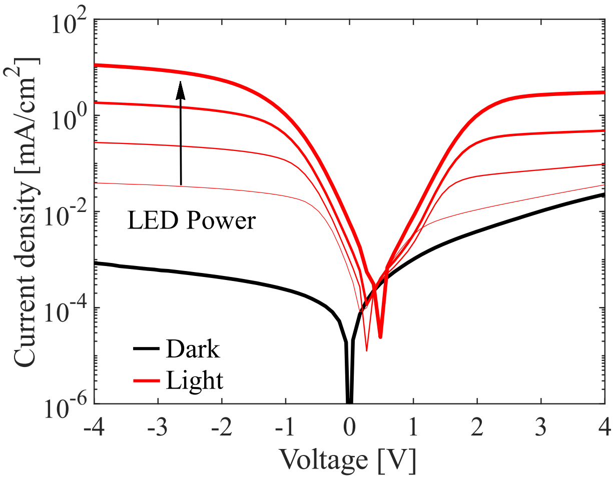

Figure S6. Measured IV curves of the OPD-CQDPD dual-band photodetector under dark and light conditions.